



CHORUS

This is the accepted manuscript made available via CHORUS. The article has been published as:

Thermal Fluctuations of Ferroelectric Nanodomains in a Ferroelectric-Dielectric $\text{PbTiO}_3/\text{SrTiO}_3$ Superlattice

Qingteng Zhang, Eric M. Dufresne, Pice Chen, Joonkyu Park, Margaret P. Cosgriff, Mohammed Yusuf, Yongqi Dong, Dillon D. Fong, Hua Zhou, Zhonghou Cai, Ross J. Harder, Sara J. Callori, Matthew Dawber, Paul G. Evans, and Alec R. Sandy

Phys. Rev. Lett. **118**, 097601 — Published 27 February 2017

DOI: [10.1103/PhysRevLett.118.097601](https://doi.org/10.1103/PhysRevLett.118.097601)

Thermal Fluctuations of Ferroelectric Nanodomains in a Ferroelectric/Dielectric PbTiO₃/SrTiO₃ Superlattice

Qingteng Zhang¹, Eric M. Dufresne¹, Pice Chen¹, Joonkyu Park², Margaret P. Cosgriff², Mohammed Yusuf³, Yongqi Dong^{4,5}, Dillon D. Fong⁴, Hua Zhou¹, Zhonghou Cai¹, Ross Harder¹, Sara J. Callori^{3*}, Matthew Dawber³, Paul G. Evans², Alec R. Sandy^{1a}

¹*X-Ray Science Division, Argonne National Laboratory, Lemont, Illinois 60439, USA*

²*Department of Materials Science and Engineering, University of Wisconsin-Madison, Madison, Wisconsin 53706, USA*

³*Department of Physics and Astronomy, Stony Brook University, Stony Brook, New York 11794, USA*

⁴*Materials Science Division, Argonne National Laboratory, Lemont, Illinois 60439, USA*

⁵*National Synchrotron Radiation Laboratory, University of Science and Technology of China, Hefei, Anhui 230026, China*

^a*Electronic mail: asandy@anl.gov*

PACS number(s): 77.80.Dj, 61.05.C-, 68.65.Cd

Ferroelectric/dielectric superlattices consisting of alternating layers of ferroelectric PbTiO₃ and dielectric SrTiO₃ exhibit a disordered striped nanodomain pattern, with characteristic length scales of 6 nm for the domain periodicity and 30 nm for the in-plane coherence of the domain pattern. Spatial disorder in the domain pattern gives rise to coherent hard x-ray scattering patterns exhibiting intensity speckles. We show here using variable-temperature Bragg-geometry x-ray photon correlation spectroscopy (XPCS) that x-ray scattering patterns from the disordered domains exhibit a continuous temporal decorrelation due to spontaneous domain fluctuations. The temporal decorrelation can be described using a compressed exponential function, consistent with what has been observed in other systems with arrested dynamics. The fluctuation speeds up at higher temperatures and the thermal activation energy estimated from the Arrhenius model is 0.35±0.21 eV. The magnitude of the energy barrier implies that the complicated energy landscape of the domain structures is induced by pinning mechanisms and domain patterns fluctuate via the generation and annihilation of topological defects similar to soft

materials such as block copolymers.

* Current Affiliation: Department of Physics, California State University – San Bernardino

Ferroelectrics exhibit a thermodynamically stable electric polarization accompanied by phenomena associated with the modification of the direction of the polarization by external fields such as stress or electric field. An important feature of ultrathin ferroelectric thin film crystals is the spontaneous formation of nanoscale polarization domain patterns in order to minimize the free energy [1]. The physical properties of the boundaries of the domains can differ significantly from the remainder of the material and the contribution of these nanodomain walls to the free energy can modify the response to applied fields [2] and the critical temperature of the ferroelectric-paraelectric phase transition [1]. Nanodomains in thin layers of ferroelectrics usually exhibit a serpentine-striped pattern [3,4], an indication of the complicated energy landscapes possibly arising from pinning mechanisms such as ion vacancies and structural defects. A crucial issue in the physics of ferroelectric nanodomains is to determine what effects govern the energy landscape for the reconfiguration of domain patterns because this landscape determines the stability and time-evolution of the domain pattern.

In a free-energy picture that depicts the free energy of ferroelectrics versus the polarization states of the entire system, in cases where the energy barriers between domain configurations are sufficiently small, the pattern reconfiguration can be driven by thermal energies. In other systems, disordered spatial structures give rise to multiple spatial patterns with energy states with small energy separations compared to $k_B T$, leading to spontaneous fluctuations in both ‘hard’ [5-7] and ‘soft’ materials [8]. However, it is technically challenging to image fluctuating ferroelectric nanodomain patterns directly because of a combination of the nm-scale periodicity of the domain pattern [3] and the pm-scale atomic displacements that distinguish domains with different polarization directions [9]. X-ray diffraction probes are sensitive to such small displacements but, with incoherent illumination, provide information about the ensemble average domain configuration allowing only the average parameters of the pattern to be determined [4,10]. Diffraction patterns generated with coherent incident x-ray beams are, however, sensitive to the instantaneous domain configuration because of the intensity speckles in the far-field diffraction

pattern [11]. Under certain conditions, particularly in domain systems exhibiting a low degree of disorder, the speckle pattern can be inverted directly to yield images of the domain configuration [12]. The serpentine-striped domain pattern considered here, however, exhibits simultaneously short periodicity and a high degree of disorder, making imaging impractical with present coherent diffraction methods. Alternatively, information about the nature and time scale of nanodomain dynamics can be gathered from fluctuations in the scattering pattern by computing the correlation function of scattering patterns acquired at a series of times.

Here we report the observation of thermal fluctuations of serpentine-striped nanodomains in a ferroelectric/dielectric superlattice via x-ray photon correlation spectroscopy (XPCS). Ferroelectric/dielectric superlattices offer the opportunity to gain precise control over the energy landscape by changing the thickness of the repeating unit of the superlattice rather than by modifying the chemical composition [13]. The scattering of coherent x-rays from the nanodomains produces a speckle pattern in which spontaneous motion of nanodomains as a function of time leads to a redistribution of the intensity among the speckles. Temporal decorrelation of the speckle pattern provides insight into the domain energetics in thermal equilibrium. Speckle patterns at all temperatures probed here exhibit a continuous decrease in the correlation coefficient as a function of elapsed time τ in a manner that can be described using a compressed exponential function $\exp[-(\tau/\tau_0)^p]$ with $p = 1.32 \pm 0.04$. The characteristic decorrelation time τ_0 decreases with increase of temperature and is consistent with our hypothesis that the equilibrium dynamics of the nanodomains is thermally activated.

Coherent x-ray scattering experiments were performed in a Bragg-diffraction geometry at beamline 8-ID-E of Advanced Photon Source using the experimental arrangement illustrated in Fig. 1(a). A series of nanodomain coherent diffuse scattering patterns were collected as a function of time at different temperatures using a charge-coupled device (CCD) x-ray detector. The sample was mounted in a custom-designed furnace for enhanced thermal stability. Vertical and horizontal slits near the sample position served as an aperture to limit the illumination to a few transverse

coherence areas. The incident x-ray beam had a photon energy 7.4 keV and was focused to 4 μm in the vertical direction using a one-dimensional compound refractive lens, producing a total flux of 3.7×10^9 photons/s. The horizontal beam size is set by the size of the horizontal slit and is 10 μm . The beam footprint on the sample was $10 \times 10 \mu\text{m}^2$ due to the Bragg reflection geometry. Details regarding the beam coherence and the speckle width can be found in the Supplemental Materials.

The ferroelectric/dielectric $\text{PbTiO}_3/\text{SrTiO}_3$ superlattice thin film was grown using off-axis radiofrequency sputtering with a repeating unit consisting of 6 unit cells of ferroelectric PbTiO_3 and 6 unit cells of dielectric SrTiO_3 . We chose a 6 $\text{PbTiO}_3/6 \text{SrTiO}_3$ superlattice because it has the highest tetragonality and therefore the strongest domain scattering intensity among superlattices with T_C below 673 K [13], a constraint imposed by the temperature range available with the furnace. The total thickness of the superlattice was 100 nm. Within this thickness, the PbTiO_3 layers are epitaxially clamped by the SrTiO_3 substrate and the polarization of the domains is parallel or anti-parallel to the surface-normal direction and is labeled ‘up’ or ‘down,’ respectively, in Fig. 1(a). A 20 nm-thick SrRuO_3 bottom electrode was grown between the superlattice and the SrTiO_3 substrate and was electrically grounded using high-temperature silver epoxy to alleviate charging effects from the x-ray radiation. All measurements were performed in air at ambient pressure.

Nanodomain x-ray scattering patterns were collected in the region of reciprocal space near the (002) Bragg reflection of the average superlattice lattice constant. Fig. 1(a) and Fig. 1(b) show the scattering geometry in real and reciprocal space, respectively. Due to the random orientation of the domain walls, the reciprocal-space average of the coherent scattering patterns illustrated in Fig. 1(b) consists of a ring of intensity around superlattice Bragg reflections. This average diffraction pattern is effectively what is observed with illumination by an incoherent incident x-ray beam. The mean period of the domain pattern and its in-plane coherence length (the average distance over which the orientation and period of the domains is constant) are $2\pi/Q^*$

and $2\pi/\Delta Q^*$, where Q^* and ΔQ^* are the reciprocal-space radius and full-width-at-half-maximum of the domain scattering ring, respectively. In x-ray measurements, each detector frame provides the distribution of intensity at the intersection of the Ewald sphere with the ring of domain diffuse scattering intensity, as illustrated in Fig. 1(b) and shown in the example of a coherent diffraction pattern in Fig. 1(c). The diffraction pattern in Fig. 1(c) was obtained by averaging 300 detector images each with an acquisition time of 10 s at temperature $T=333$ K. An estimate of the incoherent or ensemble-averaged scattering pattern to be used for the correlation coefficient calculations described below, was obtained by digitally smoothing the intensity speckles using the method described in Ref. [14] and is shown in Fig. 1(d).

Fig. 2(a) shows the temperature dependence of the intensity of the domain diffuse scattering. The contribution from the 002 Bragg reflection to the intensity distribution in Fig. 2(a) was modeled by a linear function of Q_x and subtracted from the scattering intensity. The decrease of the domain scattering intensity upon heating is apparent in Fig. 2(a) and is consistent with the decrease of the magnitude of ferroelectric polarization [15]. Fig. 2(b) and Fig. 2(c) show the peak intensity and peak position of domain scattering obtained by fitting the data to a Gaussian profile. The error bars from the Gaussian fitting are smaller than the size of the points. The decrease of the domain scattering intensity with the increase of temperature is consistent with other measurements from similar superlattices [16]. No variation of either the reciprocal-space position or width of the diffuse scattering peak is apparent within the range of temperatures probed. The periodicity and the in-plane coherence length of the domain pattern are determined from the incoherent scattering patterns to be 6.0 nm and 32.3 nm, respectively.

The equilibrium dynamics of the domains at each individual temperature can be probed using the time-dependence of the decorrelation of the coherent scattering patterns. The experimental temperature profile was chosen to eliminate artifacts associated with the long-timescale pinning of domain walls. Specifically, the experimental procedure consisted of heating to 623 K (the expected T_C according to Ref. [13]), maintaining that temperature for 10 min to

erase the thermal history of the domain pattern, and then slowly cooling to 393 K in air to ensure the maximum stability. The temperature undershoot is within 2 K and each measurement of the decorrelation was performed 45 min or more after the set temperature was reached in order to ensure thermal equilibration. Measurements performed on the static reference sample indicate that the sample environment equilibrates within about 1000 s after the set temperature is reached and is stable for at least 3000 s (see Supplemental Materials). At each temperature, 300 frames of the domain scattering patterns were collected with an acquisition time of 10 s and a wait time of 10 s with x-rays off between each frame as a precaution for radiation-induced charging effects. No significant variation of the elementary statistics of the scattering pattern, including the intensity, position, and width of the domain scattering was observed during each scan. The highest temperature probed in this study was 393 K, approximately 200 K lower than T_C [13]. Coherent scattering was impractical at higher temperatures due to the diminishing domain diffuse scattering intensity. Domain dynamics near T_C , such as those linked to the coarsening of domain structures and scaling of domain size [14], were thus not measured.

Fig. 3(a) shows the two-time correlation coefficients calculated from the domain scattering patterns at 393 K following the method described in the Supplemental Materials. The value plotted at (t_1, t_2) is the correlation coefficient between scattering patterns collected at times t_1 and t_2 . Similar two-time correlation maps were obtained at other temperatures. At each temperature, the intermediate scattering function ISF is calculated from the square root of the time average of the two-time correlation functions (Details in Supplemental Materials). The ISF at the highest temperature (393 K) can be fitted using a compressed exponential function $F(\tau) = \exp(-[\tau/\tau_0]^p)$ yielding $p = 1.32 \pm 0.04$ as the best-fit value. ISFs at other temperatures are fitted using the same p value. Characteristic times of the domain fluctuation τ_0 decrease from 26,000 s at 333 K to 7,900 s at 393 K, indicating that the rate of the domain fluctuations given by $1/\tau_0$ increases with increasing temperature. Comparison between results obtained from an

attenuated x-ray beam (half intensity) and an unattenuated beam shows no difference within the statistical uncertainty of the measurement, indicating that the decorrelation is not created by x-ray beam effects such as charging or beam-induced chemical modifications of the sample.

The temperature dependence of the characteristic time τ_0 can be used to extract the effective energy for the domain fluctuations. Fig. 4 shows the characteristic time τ_0 as a function of temperature along with a fit to the temperature dependence of τ_0 with an Arrhenius temperature dependence, $\tau_0^{-1}(T) = f_0 \exp(-E_a/kT)$. Comparison with the static reference sample (see Supplemental Materials) shows that the domains are indeed fluctuating at all temperatures considered. The larger error bars at lower temperatures are from incomplete decorrelation of the domain pattern due to the finite acquisition time of the measurements, a limit imposed by the technical difficulty of keeping the x-ray microbeam and the sample stage stable for more than a few hours at elevated temperatures. The effective activation energy E_a estimated from the Arrhenius model is 0.35 ± 0.21 eV. As a comparison, the activation energy for the migration of oxygen vacancies, a known domain wall pinning mechanism [17], is 0.8 eV in similar perovskites [18]. This oxygen vacancy energy barrier is higher than the activation energy of domain fluctuations and indicates that static arrays of oxygen vacancies are likely to become pinning sites for the fluctuation of domains. The speculation about the domain pinning sites is consistent with the compressed exponential dependence ($p > 1$) found for the ISF, which has been associated with jammed dynamics in a large number of systems including ‘soft’ [19] and ‘hard’ [5-7] materials. Specifically, for charge-density-wave domains in metallic glass, the jamming arises from collective rearrangement of domain patterns under the influence of a network of random pinning sites [5]. We therefore speculate that the complicated energy landscape of the nanodomain system is induced by static pinning mechanisms such as ion vacancies and structural defects.

Further consideration of the mechanism of the thermally activated ferroelectric

nanodomain fluctuation provides insight into the dynamical nature of fluctuating domain walls. Based on geometric considerations, it is clear that variations in the serpentine stripe patterns can occur with or without changes in the topological features. The former possibility entails the generation and annihilation of topological defects, as demonstrated in imaging studies of the motion of block copolymer chains [8]. In comparison, fluctuations without changes in the configuration require transitions between striped domains with different orientations. Ref. [20] predicts, however, that for ‘up’ and ‘down’ ferroelectric domains in a PbTiO_3 thin film grown on a SrTiO_3 substrate with similar in-plane serpentine-stripe patterns and periodicity, the free energy per unit cell for regions with the domain walls parallel to (100) direction is at least 1 meV lower than for meandering domain walls and 3 meV lower than for (110) domain walls. Based on the thickness of the repeating unit of the superlattice, the energy of (100) domain walls is at least 1.35 eV lower than that of the meandering domain walls and 4.05 eV lower than that of the (110) domain walls. Formation of (110) and meandering domain walls is therefore most likely induced by pinning mechanisms. Changes of domain wall orientation within even one domain periodicity will therefore have an energy barrier 5 to 20 times larger than the activation energy of domain fluctuations and are unlikely to contribute significantly to the observed dynamical behavior. On the other hand, the generation and annihilation of topological defects, as observed in block copolymer chains in Ref. [8], occurs via closing of the gaps between the stripes (annihilation of topological defects) and the opening of new gaps (generation of topological defects) in the immediate vicinity (usually a few stripe periods) and requires no net change of system free energy. We therefore infer that the ferroelectric domain pattern fluctuates mainly by generating and annihilating topological defects.

In conclusion, coherent synchrotron x-ray scattering from a $\text{PbTiO}_3/\text{SrTiO}_3$ superlattice shows that the serpentine striped ferroelectric nanodomains spontaneously fluctuate in thermal equilibrium. The jamming in the dynamics likely arises from pinning by static domain wall pinning mechanisms such as oxygen vacancies and structural defects. The fluctuation speeds up

at higher temperatures, yielding an effective activation energy of 0.35 ± 0.21 eV estimated from the Arrhenius model. A comparison between different models for transition states suggests that the domain patterns vary by opening and closing gaps in the stripes, leading to the generation and annihilation of topological defects with no net changes of free energy. Our study reveals the equilibrium dynamics of ferroelectric nanodomains and shows that nanoscale domain patterns introduce a new mechanism for fluctuations in ferroelectric systems. The x-ray methods we report provide a quantitative approach for measuring the stability of these structures providing essential information for both modeling and application of complex ferroelectric oxides.

This research was performed at beamline 8-ID-E of the Advanced Photon Source, a U.S. Department of Energy (DOE) Office of Science User Facility operated for the DOE Office of Science by Argonne National Laboratory under Contract No. DE-AC02-06CH11357. Work on the reference sample for the calibration of the setup stability was supported by U.S. Department of Energy, Office of Science, Office of Basic Energy Sciences, Materials Sciences and Engineering Division. Work at University of Wisconsin-Madison was supported under Grant No. DE-FG02-10ER46147 (PE). Work at Stony Brook University was supported by the U.S. National Science Foundation, Divisions of Materials Research under Grant No. 1055413 (MD).

References:

- [1] D. D. Fong, G. B. Stephenson, S. K. Streiffer, J. A. Eastman, O. Auciello, P. H. Fuoss, and C. Thompson, *Science* **304**, 1650 (2004).
- [2] G. Catalan, J. Seidel, R. Ramesh, and J. F. Scott, *Rev. Mod. Phys.* **84**, 119 (2012).
- [3] C. Thompson, D. D. Fong, R. V. Wang, F. Jiang, S. K. Streiffer, K. Latifi, J. A. Eastman, P. H. Fuoss, and G. B. Stephenson, *Appl. Phys. Lett.* **93**, 182901 (2008).
- [4] J. Y. Jo, P. Chen, R. J. Sichel, S. J. Callori, J. Sinsheimer, E. M. Dufresne, M. Dawber, and P. G. Evans, *Phys. Rev. Lett.* **107**, 055501 (2011).
- [5] J.-D. Su, A. R. Sandy, J. Mohanty, O. G. Shpyrko, and M. Sutton, *Phys. Rev. B* **86**, 205105 (2012).
- [6] S. W. Chen, H. Guo, K. A. Seu, K. Dumesnil, S. Roy, and S. K. Sinha, *Phys. Rev. Lett.* **110**, 217201 (2013).
- [7] O. G. Shpyrko, E. D. Isaacs, J. M. Logan, Y. Feng, G. Aeppli, R. Jaramillo, H. C. Kim, T. F. Rosenbaum, P. Zschack, M. Sprung, S. Narayanan, and A. R. Sandy, *Nature* **447**, 68 (2007).
- [8] L. Tsarkova, A. Knoll, and R. Magerle, *Nano Lett.* **6**, 1574 (2006).
- [9] B. Meyer and D. Vanderbilt, *Phys. Rev. B* **65**, 104111 (2002).
- [10] P. Chen, M. P. Cosgriff, Q. Zhang, S. J. Callori, B. W. Adams, E. M. Dufresne, M. Dawber, and P. G. Evans, *Phys. Rev. Lett.* **110**, 047601 (2013).
- [11] Q. Zhang, P. Chen, J. Park, M. P. Cosgriff, M. Yusuf, Z. Cai, R. Harder, S. J. Callori, M. Dawber, and P. G. Evans (unpublished).
- [12] S. O. Hruszkewycz, M. J. Highland, M. V. Holt, D. Kim, C. M. Folkman, C. Thompson, A. Tripathi, G. B. Stephenson, S. Hong, and P. H. Fuoss, *Phys. Rev. Lett.* **110**, 177601 (2013).
- [13] P. Zubko, N. Jecklin, A. Torres-Pardo, P. Aguado-Puente, A. Gloter, C. Lichtensteiger, J. Junquera, O. Stéphan, and J. M. Triscone, *Nano Lett.* **12**, 2846 (2012).
- [14] A. Fluerasu, M. Sutton, and E. M. Dufresne, *Phys. Rev. Lett.* **94**, 055501 (2005).
- [15] M. J. Highland, T. T. Fister, D. D. Fong, P. H. Fuoss, C. Thompson, J. A. Eastman, S. K. Streiffer, and G. B. Stephenson, *Phys. Rev. Lett.* **107**, 187602 (2011).
- [16] P. Zubko, N. Jecklin, N. Stucki, C. Lichtensteiger, G. Rispens, and J. M. Triscone, *Ferroelectrics* **433**, 127 (2012).
- [17] L. He and D. Vanderbilt, *Phys. Rev. B* **68**, 134103 (2003).
- [18] T. Ishigaki, S. Yamaguchi, K. Kishio, J. Mizusaki, and K. Fueki, *J. Solid State Chem.* **73**, 179 (1988).
- [19] L. Cipolletti, L. Ramos, S. Manley, E. Pitard, D. A. Weitz, E. E. Pashkovski, and M. Johansson, *Faraday Disc.* **123**, 237 (2002).
- [20] Z. Jiang, R. Zhang, D. Wang, D. Sichuga, C. L. Jia, and L. Bellaiche, *Phys. Rev. B* **89**, 214113 (2014).
- [21] M. Sutton, K. Laaziri, F. Livet, and F. Bley, *Opt. Express* **11**, 2268 (2003).

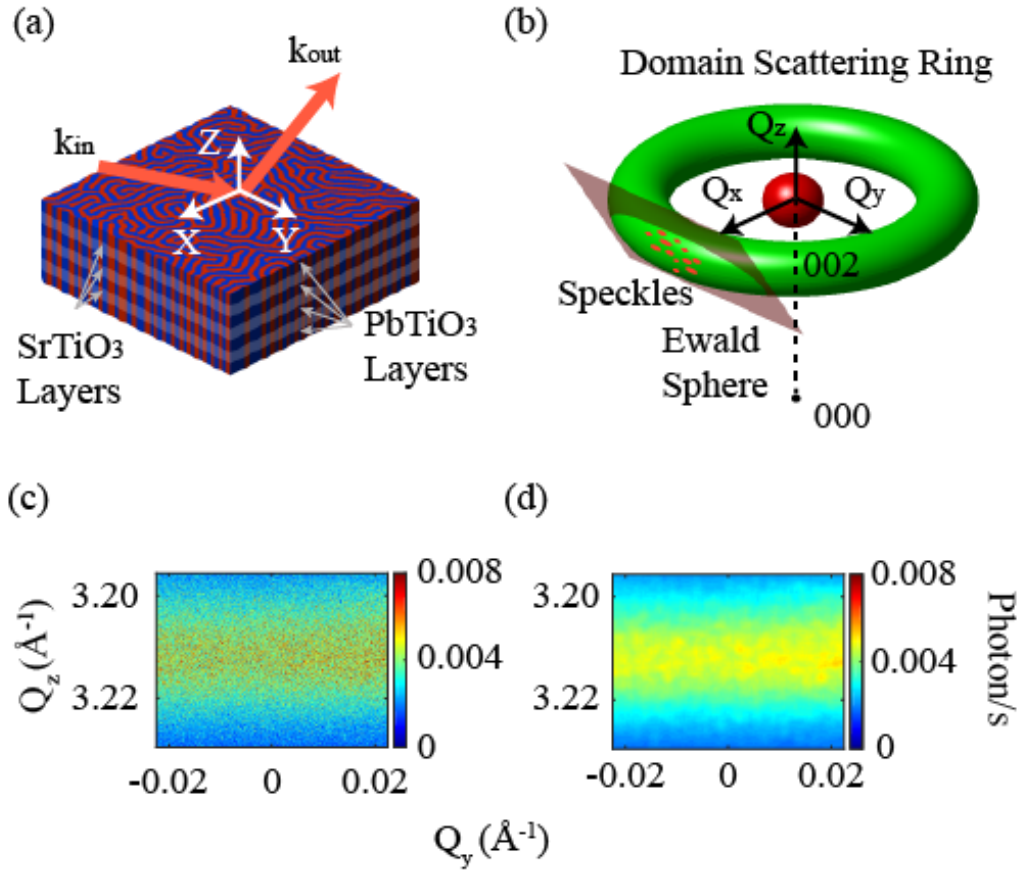


Fig. 1. (Color online) (a) The geometry of the experiment in real space. k_{in} and k_{out} represent the directions of the incident and scattered x-ray beams, respectively. The red and blue stripes in the serpentine pattern represent unit cells with ‘up’ and ‘down’ polarization in the PbTiO₃/SrTiO₃ superlattice. (b) The reciprocal-space scattering geometry. The sample and detector are arranged so that the Ewald sphere [translucent red (spherical) surface] intersects the ring of domain diffuse scattering (green ring), but does not pass through the 002 superlattice Bragg reflection (red sphere). (c) Representative coherent scattering speckle pattern from the superlattice sample. (d) Ensemble-averaged scattering pattern obtained from Fig. 1(c) via digital smoothing and used as an approximation of the incoherent scattering pattern.

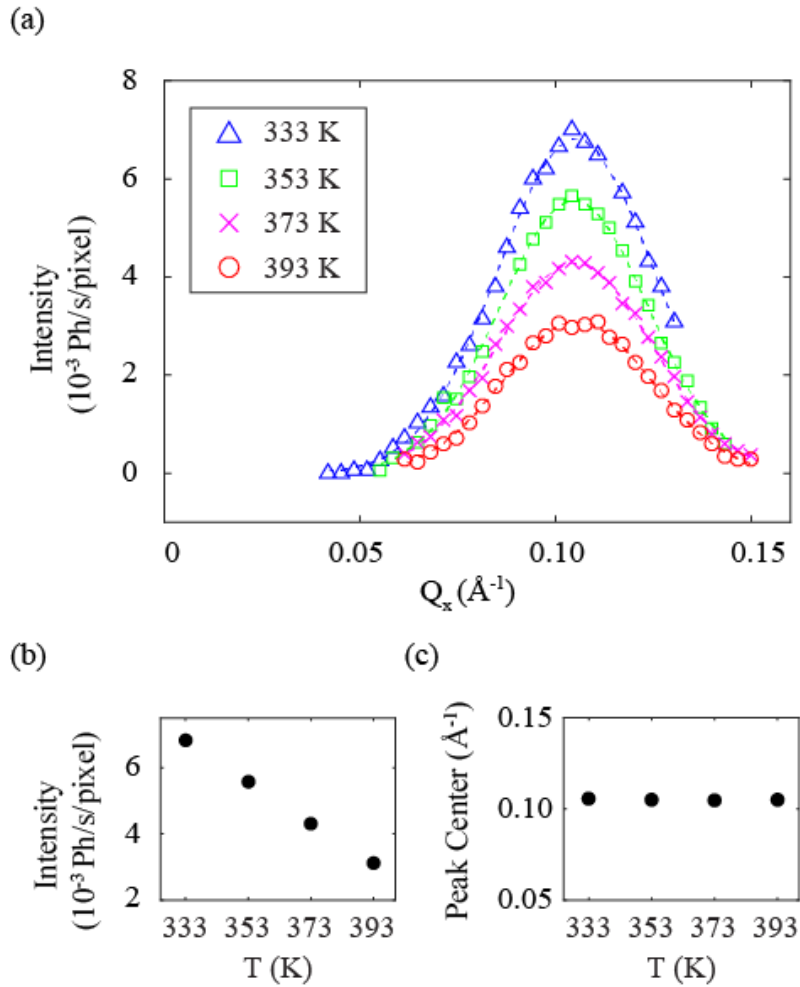


Fig. 2. (Color online) (a) Spatial profile of diffuse domain scattering intensity in reciprocal space measured from rocking curve scans at different temperatures. The dashed lines are fits to Gaussian profiles. (b). Peak intensity of the domain scattering as a function of temperature. (c). Peak position of the domain scattering (in Q_x) as a function of temperature.

Zhang *et al.*, Figure 3

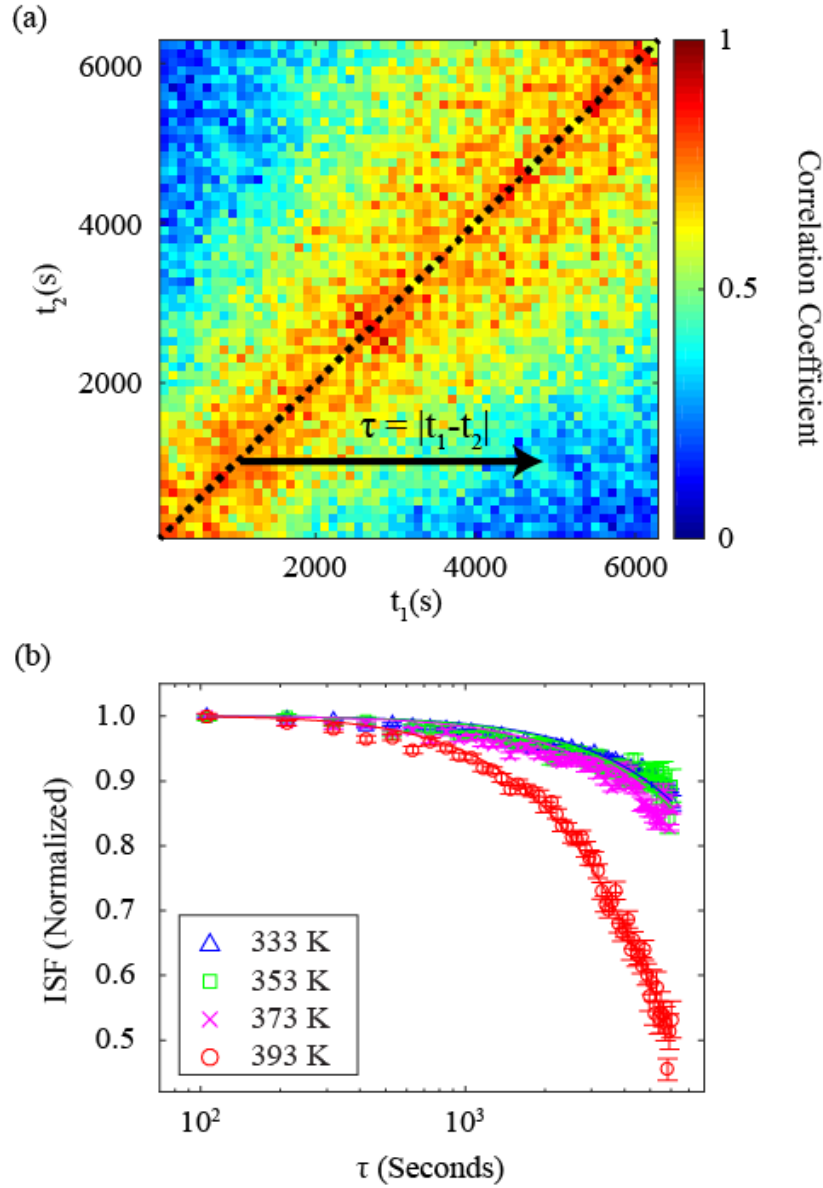


Fig. 3. (Color online) (a) Two-time correlation map for coherent domain diffuse scattering patterns at 393 K. The color scale highlights the non-diagonal values. Correlations on the exact diagonal are much higher due to self-correlation of the noise from counting statistics [21]. (b) ISFs acquired from the superlattice sample at four different temperatures. The solid lines are fits with the compressed exponential $\exp(-[\tau/\tau_0]^p)$ with $p = 1.32$.

Zhang *et al.*, Figure 4

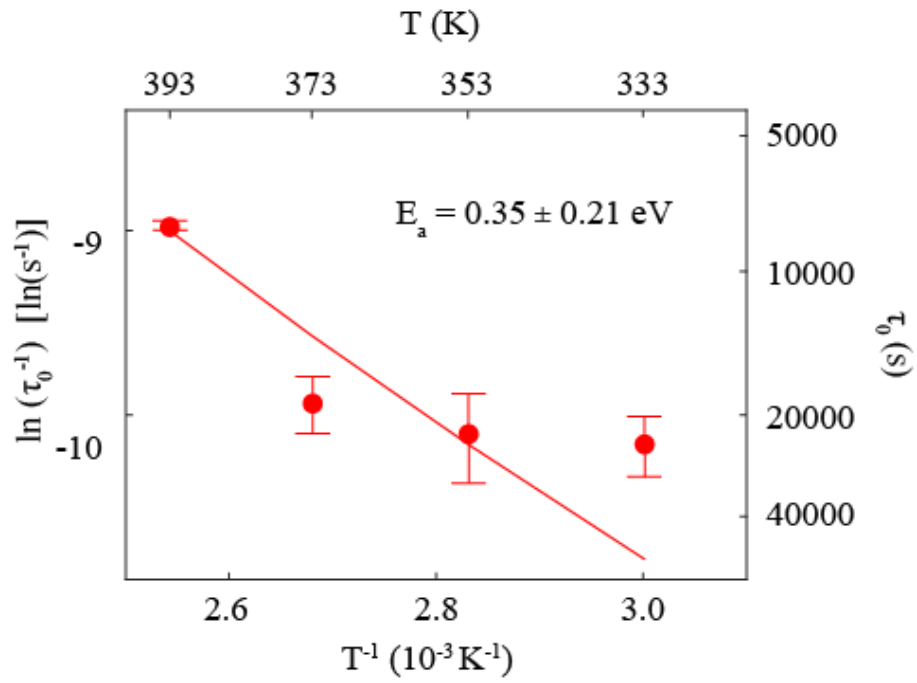


Fig. 4. (Color online) Arrhenius plot of the characteristic decorrelation time τ_0 as a function of temperature. The solid line is a fit to the Arrhenius temperature dependence.